



## Explaining Browns paradox in NdFeB magnets from micromagnetic simulations

**Bjørk, Rasmus; Insinga, Andrea Roberto**

*Published in:*  
Journal of Magnetism and Magnetic Materials

*Link to article, DOI:*  
[10.1016/j.jmmm.2023.170510](https://doi.org/10.1016/j.jmmm.2023.170510)

*Publication date:*  
2023

*Document Version*  
Publisher's PDF, also known as Version of record

[Link back to DTU Orbit](#)

*Citation (APA):*  
Bjørk, R., & Insinga, A. R. (2023). Explaining Browns paradox in NdFeB magnets from micromagnetic simulations. *Journal of Magnetism and Magnetic Materials*, 571, Article 170510.  
<https://doi.org/10.1016/j.jmmm.2023.170510>

---

### General rights

Copyright and moral rights for the publications made accessible in the public portal are retained by the authors and/or other copyright owners and it is a condition of accessing publications that users recognise and abide by the legal requirements associated with these rights.

- Users may download and print one copy of any publication from the public portal for the purpose of private study or research.
- You may not further distribute the material or use it for any profit-making activity or commercial gain
- You may freely distribute the URL identifying the publication in the public portal

If you believe that this document breaches copyright please contact us providing details, and we will remove access to the work immediately and investigate your claim.



## Research article

## Explaining Browns paradox in NdFeB magnets from micromagnetic simulations

Rasmus Bjørk<sup>\*</sup>, Andrea Roberto Insinga

Department of Energy Conversion and Storage, Technical University of Denmark (DTU), Anker Engelds Vej, 2800 Kgs. Lyngby, Denmark

## ARTICLE INFO

## Keywords:

NdFeB magnets  
Browns paradox  
Coercivity  
Maximum energy product  
MagTense  
Grain boundary

## ABSTRACT

We present the results of a systematic investigation into how the coercivity and maximum energy product of NdFeB permanent magnets are affected by magnetic and geometric microscopic properties. The results are based on numerical micromagnetic simulations carried out with the open source numerical framework MagTense. We considered artificially generated realistic microstructures for which we can control the number of crystal grains as well as the thickness of the intergrain region. Based on variations of the exchange constant, easy axis orientation, grain boundary width and intergrain material properties, the results indicate that while all of these can contribute to a reduction of coercivity, the easy axis orientation has the largest influence. For this, if the easy axis orientation is distributed within a cone with an opening angle of  $15^\circ$ , that is enough to reduce the coercivity by 1 T. Regarding the maximum energy product, the width of the grain boundary layer as well as the easy axis orientation were seen to have the largest influence, with the exchange constant only very weakly influencing the maximum energy product. Our analysis thus methodically clarifies the different factors contributing to the reduction of the value of the coercivity and maximum energy product when compared to the theoretical limit, a discrepancy known as Brown's paradox.

## 1. Introduction

At present, permanent magnets are among the most critical materials in connection to sustainable energy technologies. In fact, they are an essential element of many electro-mechanical conversion machines [1]. These can be subdivided in two main categories: electric generators, e.g. in power plants or wind turbines, and electric motors, e.g. in electric vehicles or pumps.

The most powerful permanent magnets available nowadays are composed of rare-earth elements and in particular, NdFeB magnets are the most widely used and the most powerful among permanent magnet materials [2]. However, rare-earths are expensive materials, subject to price fluctuations, and the extraction and processing is not environmentally friendly. It is thus of crucial strategic importance to explore ways of improving the performance of permanent magnet materials so that magnetic machines can be realized with lesser amount of these materials, without compromising the performance of the devices.

Micromagnetic simulations provide a very powerful tool to aid in this investigation. This mathematical formalism describes the behavior of magnetic materials at the micro-scale [3]. It can be used to predict the macroscopic magnetic properties of materials from their microstructure and composition [4]. This knowledge can in turn be

used to optimize the manufacturing process and potentially obtain better-performing materials [5].

In particular, here we focus on two macroscopic magnetic properties, namely the maximum energy product and the coercivity or coercive field. The latter is a measure of how strong an opposing field a magnet can withstand before its magnetization direction flips. In actual usage, a magnet is always subject to an opposing field which is due to other surrounding magnets and to its own demagnetizing field. Hence, the coercivity of a material defines a limit to its suitable range of applicability. The higher the coercivity, the wider is the range of possible applications, making the material more versatile. Though the use of micromagnetic simulations we in this study explore how the maximum energy product and the coercivity are influenced by the different geometrical and physical properties of the microstructure of permanent magnet materials.

This is an area that already received significant attention from the scientific community. For example, Toson et al. analyzed the coercivity of rare earth free magnets based on elongated Fe and Co nanoparticles [6]. Sepehri-Amin et al. considered the effect of size and aspect ratio of the grains on the coercivity of NdFeB sintered magnets [5,7]. Fischbacher et al. investigated how grain boundary engineering can be employed to improve the performance of NdFeB

<sup>\*</sup> Corresponding author.

E-mail address: [rabj@dtu.dk](mailto:rabj@dtu.dk) (R. Bjørk).

<https://doi.org/10.1016/j.jmmm.2023.170510>

Received 25 November 2022; Received in revised form 6 January 2023; Accepted 6 February 2023

Available online 10 February 2023

0304-8853/© 2023 The Author(s). Published by Elsevier B.V. This is an open access article under the CC BY license (<http://creativecommons.org/licenses/by/4.0/>).

magnets [4]. Kovacs et al. explored enhancement of the performance through nano-structuring of rare earth free magnets [8]. The study by Lee et al. reports on the effect of the grain-boundary phase on the nucleation mechanism and domain-wall motion [9]. Hoyun et al. consider the coercivity of AlNiCo and how it is affected by dimensions and geometry [10].

The novelty of our study is that we systematically analyze the impact of all the main microstructural features on the coercivity and maximum energy product. Specifically, we investigate how the different factors are responsible for the observed reduction of the coercivity with respect to the maximal theoretical value. We show the dependence of the coercivity on the strength of the exchange interaction, the dependence on the misalignment between the easy axes of the different crystal grains composing the microstructure and the dependence on the thickness and the magnetic properties of the secondary phase that is present at the boundary between adjacent grains.

This investigation advances the understanding of the relation between the structure of permanent magnets and their macroscopic behavior, i.e. their performance. Thus, it suggests the most promising directions for future research aimed at developing manufacturing processes for stronger permanent magnet materials. All our results have been obtained with the computational framework MagTense [11], which has been extensively validated [12] with the  $\mu$ MAG standard micromagnetic problems [13]. The results of additional validation tests are included in the present work.

## 2. Model

### 2.1. Governing equations

At the nano- and micro-scale, the behavior of magnetic materials can be modeled by considering the formalism of micromagnetics. Here, the magnetic state of the system is described by the vector field  $\mathbf{M}(\mathbf{x})$ , i.e. the magnetization spatial variation. Here  $\mathbf{x}$  denotes a vector corresponding to a generic point of space inside the region  $\Omega$  occupied by the magnetic material. The time-evolution and the equilibrium configurations of the systems are determined by the micromagnetic free energy  $\mathcal{G}$ , which is a function of  $\mathbf{M}(\mathbf{x})$ .

As explained below, the equation governing the time evolution of  $\mathbf{M}(\mathbf{x})$  conserves the norm  $\|\mathbf{M}\|$  at any point, since this is assumed to be a fixed (local) property of the material. Therefore, it is customary to introduce the quantity  $M_s(\mathbf{x})$ , referred to as saturation magnetization, which corresponds to the magnitude of  $\mathbf{M}$  at the point  $\mathbf{x}$ . The state of the system is thus naturally expressed by the reduced magnetization  $\mathbf{m}$  defined by:

$$\mathbf{m}(\mathbf{x}) = \frac{\mathbf{M}(\mathbf{x})}{M_s(\mathbf{x})} \quad (1)$$

The micromagnetic free energy  $\mathcal{G}$  is expressed as the integral over the region  $\Omega$  of a corresponding energy density function  $g$  that depends on  $\mathbf{m}(\mathbf{x})$ , and on its spatial derivatives:

$$\mathcal{G}[\mathbf{m}] = \int_{\Omega} dV g(\mathbf{m}, \nabla \mathbf{m}) \quad (2)$$

The time-evolution equation is expressed in terms of the *effective field* which is proportional to the functional derivative of  $\mathcal{G}$  with respect to  $\mathbf{m}$ :

$$\mathbf{H}_{\text{eff}} = -\frac{1}{\mu_0 M_s} \frac{\delta \mathcal{G}}{\delta \mathbf{m}} \quad (3)$$

where  $\mu_0$  indicates the vacuum permeability. The time-evolution of the system is described by the Landau–Lifshitz equation [4]:

$$\frac{d\mathbf{m}}{dt} = -\gamma \mathbf{m} \times \mathbf{H}_{\text{eff}} - \alpha \mathbf{m} \times (\mathbf{m} \times \mathbf{H}_{\text{eff}}) \quad (4)$$

The equation is parametrized by the gyromagnetic ratio  $\gamma$  and damping parameter  $\alpha$ . Since the time derivative of  $\mathbf{m}$  is perpendicular to  $\mathbf{m}$  at any point, the norm of  $\mathbf{m}(\mathbf{x})$  is conserved. The first term on the

**Table 1**  
Physical mechanisms.

Physical mechanism	Energy density	Effective field
External field	$-\mu_0 M_s (\mathbf{m} \cdot \mathbf{H}_a)$	$\mathbf{H}_a$
Demagnetization	$-\left(\frac{\mu_0 M_s}{2}\right) (\mathbf{m} \cdot \mathbf{H}_d)$	$\mathbf{H}_d$
Exchange	$A_0 \sum_j \ \nabla \mathbf{m}_j\ ^2$	$\left(\frac{2A_0}{\mu_0 M_s}\right) \sum_j \frac{\partial^2 \mathbf{m}}{\partial x_j^2}$
Anisotropy	$-K_0 (\mathbf{m} \cdot \hat{\mathbf{e}}_K)^2$	$\frac{2K_0}{\mu_0 M_s} (\mathbf{m} \cdot \hat{\mathbf{e}}_K) \hat{\mathbf{e}}_K$

right-hand side of Eq. (4) causes the vector  $\mathbf{m}(\mathbf{x})$  to precess around the effective field  $\mathbf{H}_{\text{eff}}(\mathbf{x})$ , while the second term causes  $\mathbf{m}(\mathbf{x})$  to rotate towards  $\mathbf{H}_{\text{eff}}(\mathbf{x})$ . At equilibrium,  $\mathbf{m}$  is aligned to the effective field at any point, as expressed by Brown's equation:

$$\mathbf{m}_{\text{eq}} \times \mathbf{H}_{\text{eff}} = 0 \quad (5)$$

The expression of the micromagnetic free energy  $\mathcal{G}$  includes different physical mechanisms, each corresponding to a different energy term. The four main mechanisms are: the external field energy, the demagnetization energy, the exchange interaction, and the crystal anisotropy. For each of the energy terms, a corresponding effective field is constructed. The energy density functions  $g$  and associated effective fields are listed in Table 1.

In the table,  $K_0$  denotes the anisotropy constant,  $\hat{\mathbf{e}}_K$  is a unit vector pointing in the direction of the easy (or hard) crystallographic axis,  $A_0$  denotes the exchange interaction constant,  $\mathbf{H}_a$  is the applied magnetic field, and  $\mathbf{H}_d$  is the demagnetization field. The index  $j$  runs over the spatial coordinates  $x$ ,  $y$  and  $z$ . The demagnetization field is the field generated by the magnetic material in  $\Omega$  and is expressed in terms of the rank-2 demagnetization tensor  $\underline{\underline{\mathcal{N}}}$ :

$$\mathbf{H}_d(\mathbf{x}) = \int_{\Omega} dV' \underline{\underline{\mathcal{N}}}(\mathbf{x}, \mathbf{x}') \mathbf{M}(\mathbf{x}') \quad (6)$$

Besides the four physical mechanisms mentioned above, the same formalism can also be applied to model other effects. One example is the simulation of thermal fluctuations, which may be included as discussed in Refs. [4,14]. However, in this work we do not explicitly consider thermal effects since these can be well approximated by including a thermal fluctuation term directly in the results [4].

In this work we focus on permanent magnet materials, and specifically on magnetic hysteresis curves. These curves describe the dependence of the equilibrium magnetic state as function of a time-varying applied magnetic field  $\mathbf{H}_a$ . The rate of variation of the field is assumed to be slow enough that the system can realistically be assumed to be quasi-statically following the equilibrium state [15].

Fig. 1(a) shows an illustrative example of a typical hysteresis curve. We consider a situation where the permanent magnet is initially uniformly magnetized in the direction of the external field. The applied field is then decreased until it eventually reverses, i.e. it points in the opposite direction with respect to its initial orientation. During this process, the magnet will be able to maintain its original magnetized state until the opposing field becomes too intense and the magnetization direction of the material eventually reverses as well. The value of applied field corresponding to this magnetization-reversal process is known as the *coercive field* and indicated by  $H_c$ .

As discussed in the introduction, the goal of this study is to investigate the dependence of  $H_c$  and the maximum energy product,  $(BH)_{\text{max}}$ , on the different physical parameters and on the geometrical features of the microstructure of polycrystalline permanent magnet materials. For this purpose, we employ the micromagnetic numerical simulation framework MagTense [11].

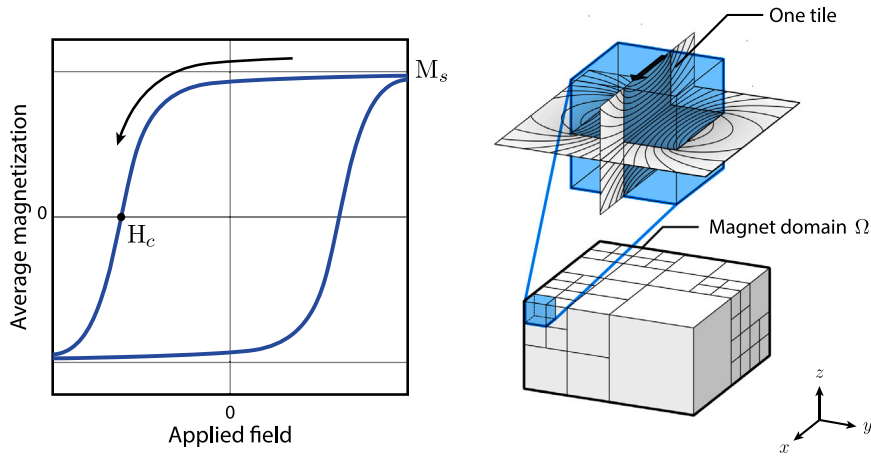


**Fig. 1.** (a): Example of hysteresis curve of permanent magnet material. The coercive field,  $H_c$ , corresponding to the intersection of the curve with the horizontal axis, is shown. (b): Example of mesh used to discretize the governing equations. The mesh-elements can have different sizes. The total demagnetization field is obtained by adding the analytically-computed contributions from all the mesh-elements, each assumed uniformly magnetized.

## 2.2. Numerical framework

In MagTense, the governing equations are discretized by subdividing the region  $\Omega$  into a number of mesh-elements, each of which is assumed to be uniformly magnetized. An example of a typical mesh is shown in Fig. 1(b). As can be noticed, the mesh elements do not need to be identical to each other. Section 2.3 includes additional details on the mesh-generation procedure. The mesh-elements will also be referred to as “tiles”.

The demagnetization field in any point  $\mathbf{x}$  is obtained by superimposing the analytically-computed contributions from all the mesh-elements [12]:

$$\mathbf{H}_d(\mathbf{x}) = \sum_n \underline{\mathcal{N}}_n(\mathbf{x}) \mathbf{M}_n \quad (7)$$

where  $\mathbf{M}_n$  denotes the magnetization of the  $n^{\text{th}}$  tile and  $\underline{\mathcal{N}}_n(\mathbf{x})$  denotes the demagnetization tensor of the  $n^{\text{th}}$  tile evaluated at the point  $\mathbf{x}$ . The summation runs over all the tiles composing the mesh.

As compared to the MagTense modeling framework published previously [12], the version presented here has furthermore been modified to include averaging of the magnetic field within each tile, instead of evaluating this only at the center of the tile. The magnetic field generated by a uniformly magnetized tile  $R_n$  should ideally be evaluated over the whole receiving tile  $R_{n'}$ . In principle, the analytical expression for the field averaged over the receiving tile can be found by the volume integration of the analytical expression for the demagnetization tensor across the receiving tile  $R_{n'}$  as

$$\langle \mathbf{H}_d \rangle_{R_{n'}} = \frac{1}{V'} \int_{R_{n'}} dV \mathbf{H}_d(\mathbf{x}) = \langle \underline{\mathcal{N}}_n \rangle_{R_{n'}} \mathbf{M}_n \quad (8)$$

where  $V'$  denotes the volume of the receiving tile, and  $\langle \underline{\mathcal{N}}_n \rangle_{R_{n'}}$  is defined as

$$\langle \underline{\mathcal{N}}_n \rangle_{R_{n'}} = \frac{1}{V'} \int_{R_{n'}} dV \underline{\mathcal{N}}_n(\mathbf{x}) \quad (9)$$

However, the analytical expressions for the demagnetization tensor cannot easily be integrated. Closed-form expressions have been reported for a grid of identical cubic tiles and also for a mesh of prisms, as long as the faces are parallel [16]. Instead, here we employ the approach of computing the average demagnetization tensor across each tile by calculating the tensor for a finite number of points in each tile and then performing the average. This is a valid approximation as long as the mesh resolution is sufficient. As demonstrated in Ref. [12], the model is already able to reproduce the  $\mu\text{mag}$  standard problem results simply by evaluating the field at a single point in the center of the tile, provided that the resolution is suitable.

As seen in Table 1, the effective field associated to the exchange interaction involves the calculation of the Laplace operator applied to  $\mathbf{m}(\mathbf{x})$ . In our framework the Laplace operator is computed by considering a generalization of the finite-difference method that is applicable to arbitrary unstructured meshes. Ref. [17] discusses in details the construction of the Laplace operator and the implementation of the correct boundary conditions at the external boundaries, and at the interface between regions characterized by different values of  $A_0$ .

## 2.3. Geometry and mesh

Our goal is investigating the behavior of sintered polycrystalline permanent magnet materials, most prominently NdFeB magnets. The microstructure of these materials is composed by a number of crystal grains of hard-ferromagnetic NdFeB phase, separated from each other by a thin layer of intergrain phase. This phase will also be referred to as the grain boundary phase.

An example of such a microstructure is shown in Fig. 2(a). Here, the different NdFeB grains are indicated by different colors, while the intergrain phase is not shown. The structure has been generated by constructing a Voronoi tessellation. This procedure allows us to control the shape and size of the magnet, the number of grains, and the thickness of the intergrain region.

Following the generation of the microstructure, a mesh is realized by employing an iterative refinement scheme. The procedure starts with a regular Cartesian mesh with given resolutions along the  $x$ ,  $y$ , and  $z$  directions. At each step of the iteration, all the tiles that lie (partially or entirely) in the intergrain region are subdivided into 8 smaller identical tiles by bisecting the original tile along each spatial dimension. Fig. 2(b) shows the mesh corresponding to the microstructure shown in Fig. 2(a). The mesh has been constructed by performing 3 refinements steps on a mesh with base resolution  $5 \times 5 \times 5$ . As discussed in Ref. [17], the construction of the Laplace operator for such an irregular mesh involves choosing the exponent of a distance weight factor, here taken to be 6 in accordance with the aforementioned reference.

## 2.4. Model and material parameters

For the purpose of calculating hysteresis curves, we assume quasi-static conditions. In this regime, it is not necessary to include the precessional term in the Landau–Lifshitz equation, i.e. Eq. (4), and we therefore set  $\gamma = 0 \text{ m/(As)}$ . For each hysteresis curve, we vary the external field starting from 1 T and until the coercivity of the magnet has been exceeded. The steps in field are 0.1 T unless otherwise stated. At each step, the system is allowed to relax to the new equilibrium

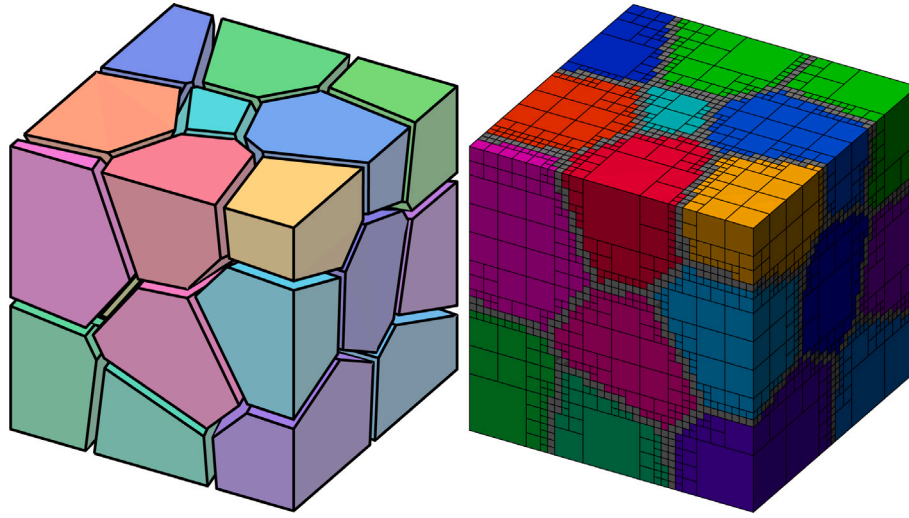


**Fig. 2.** (a): The grain structure considered: a cube with side-length 240 nm, 25 grains, and grain boundary width  $\delta_{GB} = 7.5$  nm. (b): The corresponding mesh has a base resolution of 5 tiles along each spatial dimension and has been successively refined 3 times.

**Table 2**  
Material parameters.

Material	Parameter	Quantity
NdFeB grains	$\mu_0 M_s$	1.61 T
	$A_0$	$7.7 \times 10^{-12}$ J/m
	$K_0$	$4.3 \times 10^6$ J/m <sup>3</sup>
Intergrain phase	$\mu_0 M_s$	0.50 T
	$A_0$	$7.7 \times 10^{-12}$ J/m
	$K_0$	0 J/m <sup>3</sup>

value. This is performed by numerically integrating the Landau–Lifshitz equation from 0 to 40 ns with the value of the damping parameter  $\alpha$  set to 4000 m/(As).

In order to model the NdFeB and intergrain phases, we consider the two sets of properties for the saturation magnetization,  $\mu_0 M_s$ , the exchange constant,  $A_0$  and the anisotropy constant,  $K_0$ , listed in Table 2.

For the values of these parameters, we follow the work by Fischbacher et al. [4]. Moreover, it is worth mentioning that in a modeling study of melt-spun NdFeB magnets Toson et al. [6] used a very similar set of material parameters for NdFeB:  $\mu_0 M_s = 1.61$  T and  $A_0 = 7.7 \times 10^{-12}$  J/m and  $K_0 = 4.9 \times 10^6$  J/m<sup>3</sup>. These are identical to the parameters used here, except for a slightly larger anisotropy constant. In the same work, three different magnetic grain boundary phases were modeled. The soft-ferromagnetic phase, which is the most similar to the one used here has the following properties  $\mu_0 M_s = 0.75$  T,  $A_0 = 2.5 \times 10^{-12}$  J/m and  $K_0 = 0$  J/m<sup>3</sup>, again very close to the values used in this study. These values agree with values determined from experiments [18–20] as also argued by Toson et al. [6].

The theory of micromagnetics predicts that the possible values of coercive field are limited by a maximum attainable value, known as the nucleation field [4,21]. The nucleation field is defined as:

$$H_N = \frac{2K_0}{M_s} \quad (10)$$

With the parameters used in this work for the NdFeB crystal grains, the maximum coercive field expressed in teslas is thus  $\mu_0 H_N = 6.71$  T. Correcting for shape demagnetization, the nucleation field becomes [22]

$$H_N = \frac{2K_0}{M_s} - N \frac{M_s}{\mu_0} \quad (11)$$

where  $N$  is the shape demagnetization factor. As we here consider a cubed sample we have  $N = 1/3$ , giving a nucleation field of  $\mu_0 H_N = 6.18$  T.

## 2.5. Easy axis direction

As discussed in the previous section, we assume that the NdFeB grains are characterized by identical values for  $K_0$ ,  $A_0$  and  $M_s$ . However, the crystallographic orientation can be different in different grains. This situation is modeled by considering a different easy-axis vector  $\hat{e}_K$  for each grain. It is important to stress that since we are considering uni-axial anisotropy, the directions  $\pm \hat{e}_K$  are equivalent.

For each grain, the easy axis is generated randomly on a spherical cap centered on the  $[0,0,1]$  direction, i.e. along the  $z$  axis, which is also the direction of the applied field. The opening angle of the spherical cap is defined as half the full opening angle of the spherical cap, i.e. as shown in Fig. 3. Thus, when the cone opening angle  $\theta_{\text{cone}}$  is  $90^\circ$ , the easy axis directions are uniformly distributed across the northern hemisphere of the unit circle. When considering the uni-axial symmetry, this corresponds to a completely isotropic random distribution. On the opposite situation, when  $\theta_{\text{cone}} = 0^\circ$ , the easy axis points along the  $z$  direction in all the grains.

We also consider the special case of the easy axis being located only on the edge of the spherical cap defined above. Thus in this case, a cone edge angle of  $90^\circ$  corresponds to a situation where for all the grains the easy is perpendicular to the  $z$  direction, i.e. perpendicular to the direction of the applied field.

Finally, we note that the centered spherical cap considered as the base case is defined such that no angles are found outside the spherical cap. A true physical distribution would most likely be more normally distributed, so therefore we also consider a case where the easy axis orientations are normally distributed on the sphere centered on the  $[0,0,1]$  direction and with the standard deviation given by the opening angle of the spherical cap.

## 3. Model validation

We consider the effect of different geometrical and magnetic parameters on the hysteresis curves and the corresponding coercivity and energy product. In order to ensure that the investigation is performed systematically, the starting model is always the same, except for the parameter being varied in each section. The geometry of the starting model is shown in Fig. 2, and we term this the base case. It consists of a cubic magnet with side-length equal to 240 nm along each direction, similar to the system studied in Ref. [4], and comparable to the  $(200 \text{ nm})^3$  system studied in Ref. [6]. The cube is subdivided into 25 crystal grains, with a grain-boundary base thickness of 7.5 nm. The



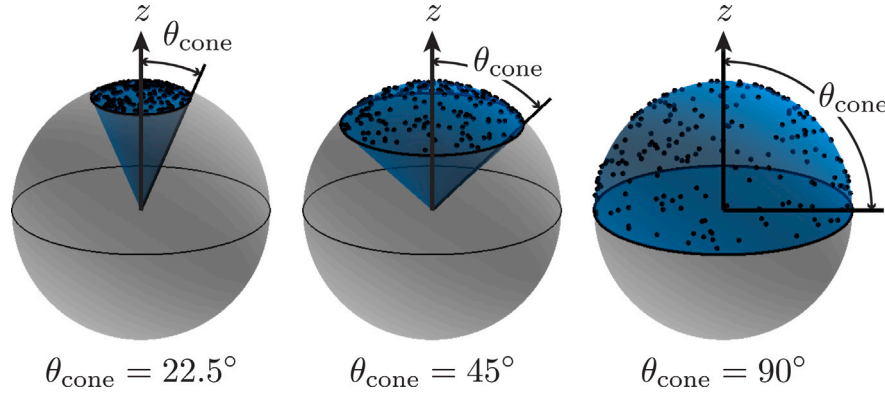


Fig. 3. The definition of the cone opening angle,  $\theta_{\text{cone}}$ , which parametrizes the random distribution of the easy axis orientation among the different crystal grains.

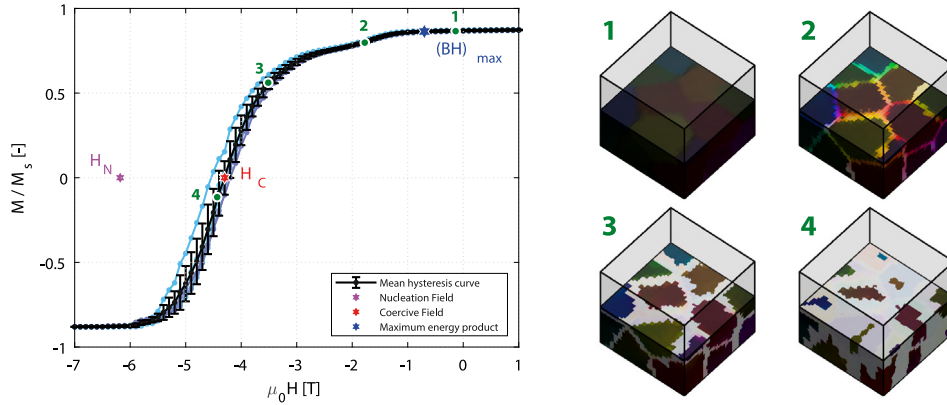


Fig. 4. (a) The hysteresis curve for the base case. The mean hysteresis curve is an average of five simulations with randomized cone angles. These are plotted behind the curve in the plot. (b) Magnetization states for four intermediate steps of one of the five simulations. The color indicate the direction of the magnetization at any point: black and white indicate the positive and negative  $z$  direction, respectively, while the colors of the rainbow indicate in-plane magnetization. For example, in the first step, the magnetization points roughly in the  $z$  direction, although there is a small in-plane component, which is different for each grain. The steps corresponding to these four intermediate states are indicated in the left panel as green circles.

base properties are listed in Table 2. The cone opening angle of the easy axis distribution is  $\theta_{\text{cone}} = 15^\circ$ . We perform five simulations with the same grain structure but different randomized easy axis orientation within the defined  $\theta_{\text{cone}} = 15^\circ$ . The mean hysteresis curve for these five simulations is shown in black in Fig. 4(a) with mean value of the coercivity of  $\mu_0 H_c = -4.32 \pm 0.2$  T and  $(BH)_{\text{max}} = 385 \pm 3$  kJm $^{-3}$ . The individual curves corresponding to the five simulations are also shown, indicated by the colored curves. Fig. 4(b) shows the magnetization states corresponding to the four intermediate steps shown in (a) as green circles. As can be observed, the grain boundary phase undergoes magnetization-reversal before the NdFeB phase. Subsequently, the demagnetized front expands inwards until all the grains are reversed.

### 3.1. Model sensitivity verification

In order to verify the grained model, we considered the base model, but with zero grain boundary thickness and cone opening angle of the easy axis orientation of  $\theta_{\text{cone}} = 1^\circ$ . Ten simulations were conducted and the mean coercivity was calculated to be  $\mu_0 H_c = -5.52 \pm 0.02$  T. Following this, ten simulations with a regular grid, i.e. where all tiles are the same size and there are no grains, were conducted. Here the exchange operator is calculated using a standard finite difference method [12]. The mean of the coercivity for these models are  $\mu_0 H_c = -5.57 \pm 0.04$  T, which is very close to the grained models. This establishes that the grained model correctly calculate the coercivity of a given sample.

Returning to a model with grain boundaries, in order to confirm a correct selection of the time interval for integration, field stepping for the hysteresis curve and weight factor for the exchange operator, we

performed a simulation of the base case, where the time integration was changed to 120 ns, the field stepping was made to be 0.05 T and the weight scheme was changed to 8 for the exchange calculation. Furthermore, for this simulation we also averaged the  $\underline{N}$ -tensor over  $4 \times 4 \times 4$  evenly distributed points in each tile, as discussed in Eq. (9). This test resulted in a coercivity of  $\mu_0 H_c = -4.29$  T, very similar to the value of the coercivity of the base case given above.

Finally, to ensure that the exchange calculations were done correctly, a simulation was run where the Green-Gauss method was instead used to calculate the exchange matrix operator, but otherwise using the standard parameters defined above. This resulted in a coercivity of  $\mu_0 H_c = -4.50$  T. This is again quite close to the result obtained with the standard Direct Laplacian method, which anyway is expected to be the most accurate of the two approaches [17].

## 4. Results of a multigrain system

In the following subsections we will consider how the coercivity,  $H_c$ , and maximum energy product,  $(BH)_{\text{max}}$ , for a multigrain NdFeB system depend on the geometrical and microstructural parameters. We study how the exchange constant  $A_0$ , easy axis orientation,  $\theta_{\text{cone}}$ , grain boundary width,  $\delta_{\text{GB}}$ , and grain boundary material properties affect the coercivity and the maximum energy product. In all cases, the starting configuration is the base model discussed above.

The coercivity and the maximum energy product are both calculated from the computed hysteresis curves. The coercivity is interpolated as the value of applied field at which the magnetization in the direction of the applied field is zero. The maximum energy product is interpolated

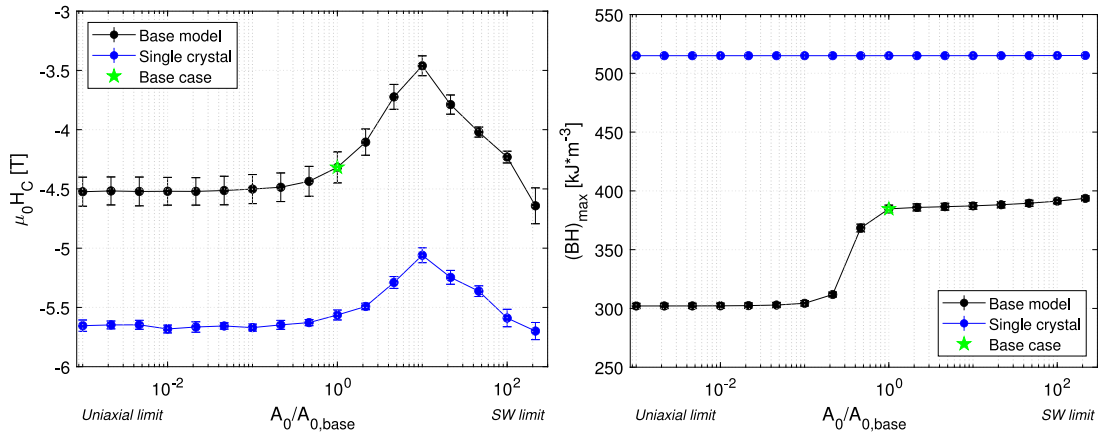


Fig. 5. (a) The coercivity and (b) the maximum energy product as function of  $A_0$  normalized by  $A_0$  of the base model, respectively. The legend indicates the system studied. The error bars indicate the standard deviation of the five simulations with randomized easy axis orientations as described in the text used to compute the average value.

as the value at which the negative product of the magnetic field and the magnetic flux density is maximized. The magnetic flux density is calculated as  $\mathbf{B} = \mu_0(\mathbf{H} + \mathbf{M})$ . In the following,  $H_c$  and  $(BH)_{max}$  will be presented directly as results. The hysteresis curves are not shown for brevity but can be obtained from the data repository for this work, as described in the data availability section.

#### 4.1. Exchange interaction strength

We first consider a case that can somewhat be compared with the well-known Stoner–Wohlfarth model, which describes the hysteresis curve for uniformly magnetized particles, i.e. where the exchange interaction is dominating, thus preventing magnetization gradients from occurring. For this purpose, we return to the base model properties and mesh introduced at the beginning of Section 3, which is also used in the next sections. To understand the influence of the exchange interaction strength,  $A_0$ , not only for the base case, we additionally also consider a single-crystal magnet. For this we take a cone opening angle of the easy axis orientation to be  $\theta_{cone} = 1^\circ$  and a grain boundary width of  $\delta_{GB} = 0$  nm.

We simultaneously increase  $A_0$  for both the NdFeB and the inter-grain phase. As  $A_0$  increases, the steps in external field in the hysteresis curve is decreased to ensure convergence of the simulations, as was also done for solutions to the  $\mu\text{mag}$  standard problem 2 published previously [12]. The convergence criteria used was that the coercivity had to change less than 0.01 T when decreasing the field steps in half. For the exchange interaction strength equal to  $1A_0$  and  $2.2A_0$  the field step was 0.1 T, at  $4.6A_0$  the field step was 0.02 T, at  $10A_0$ ,  $21A_0$  and  $46A_0$  the field step was 0.01 T, at  $100A_0$  it was 0.005 T and finally at  $215A_0$  it was 0.001 T.

The calculated coercivity and maximum energy product averaged over five simulations with randomized easy axis directions are shown in Fig. 5. The base model corresponds to the black dots, and the single crystal to the blue dots. As expected, when  $A_0$  becomes large, i.e.  $A_0 > 10^1$ , the value of the coercive field increases significantly. This is caused by the system being dominated by exchange interactions and the value of the coercivity approaches the Stoner–Wohlfarth limit, although this value is not reached here due to the excessive convergence criteria at high  $A_0$  values.

In the opposite case as  $A_0$  is reduced, i.e.  $A_0 > 10^{-1}$ , the coercivity becomes dominated by the uni-axial anisotropy of the grains and thus stabilizes. The value obtained for the choice of  $A_0$  used for the base model is indicated by the star marker. The drop in maximum energy product seen for the base model when  $A_0$  is decreased is caused by a reversal of the grain boundary phase. With lower  $A_0$  the coupling between the grains and the grain boundary becomes weaker, causing the grain boundary to reverse earlier, until it reverses before the maximum energy product is reached.

#### 4.2. Easy axis misalignment

Next we consider the influence of the easy axis orientation on the coercivity and the maximum energy product. As discussed previously, the easy axis orientation is randomized within a specified cone opening angle. We consider both the base case model, as well as a similar system but without a grain boundary phase, i.e.  $\delta_{GB} = 0$ , as well as cases where the easy axis orientation has to be located on the cone edge or are normally distributed, as also described previously. Shown in Fig. 6 is the coercivity and the maximum energy product as function on the cone opening angle of the easy axis direction. A total of five simulations, each with random easy axis generated for the chosen cone opening angle, has been conducted to provide a statistical measure on the certainty of the results. The error bar shows the standard deviation within the five simulations with the same cone opening angle.

As can be seen from the figure, the size of the error bars increases as the cone opening angle widens. This is expected, as the randomness in the easy axis orientation becomes larger with the cone opening angle. The coercivity decreases significantly with the cone opening angle, until at a fully randomized cone angle  $\theta_{cone} = 90^\circ$  for the case of the easy axis orientation being on the edge of the cone, the coercivity and maximum energy product become zero. This result is expected, since in this situation all the easy axes of the various grains point in directions perpendicular to the applied field. It is also seen that the normally distributed angles result in a worse coercivity and maximum energy product compared to the base case. This is because in the normally distributed case there is simply more variation in the easy axis orientations, resulting in more grains with an easy axis orientation more perpendicular to the applied field. Finally, the difference between a multigrain structure with and without grain boundary is seen to be small.

The trend observed in this work, namely that the coercivity increases with alignment of the easy axis orientation to the direction of the applied field, is opposite to the magnetostatic regime calculation where the opposite effect occurs, namely that coercivity increases as the angle between the easy axis orientation and the applied field increases. In the magnetostatic limit this occurs because the coercivity is the average coercivity of the individual grains in the ensemble. For a single large particle with an easy axis, if there is an angle between the applied field and the easy axis, then the projection of the applied field onto the easy axis orientation will obviously be smaller than the full applied field. As the vector projection is smaller, a larger applied field is needed to overcome the coercivity in the easy axis orientation. This is also seen experimentally for NdFeB magnets with large grains, 3–5  $\mu\text{m}$  [23].

However, in this work, we explore the limit of much smaller NdFeB grains, which thus are much more tightly interacting due to the exchange coupling. This causes the different trend in the orientation

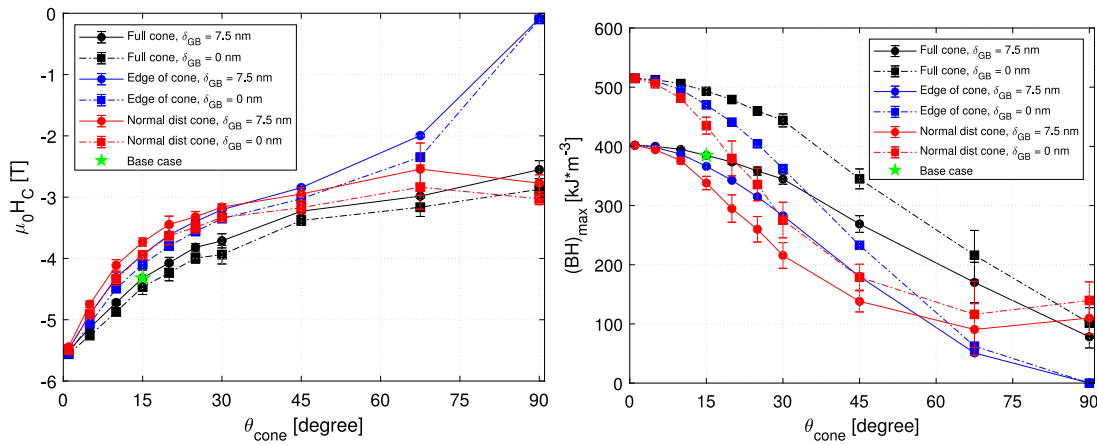


Fig. 6. (a) The coercivity and (b) the maximum energy product as function of the cone angle for both the standard uniform full cone orientation, for the case where the easy axis can only be located on the edge of the cone, and for the normally distributed case, as defined in Section 2.5.

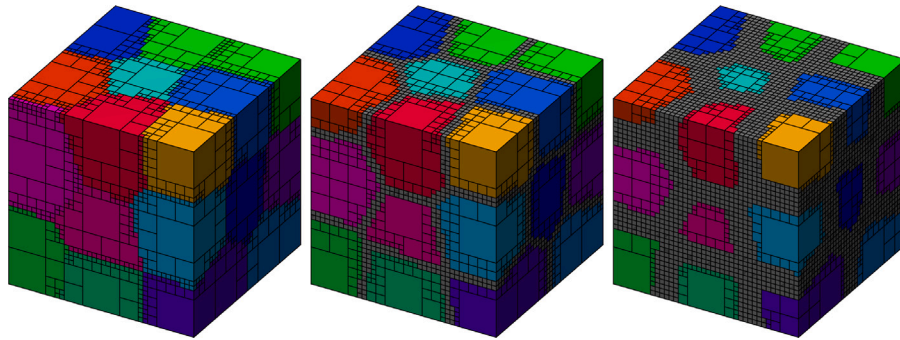


Fig. 7. The base case with a grain boundary of 0 nm, 10.5 nm and 31.5 nm, respectively.

investigation seen here. That systems with small NdFeB grains have an increasing coercivity compared to systems with larger grains have been observed experimentally [24,25], although this was not investigated for different applied field orientations.

Another issue worth remarking is that an investigation by Suss et al. (2000) showed that if a micromagnetic grain model system is free of defects coercivity increases with an increased easy axis alignment, which is also in agreement with the Stoner–Wolfarth model [26]. However, coercivity will decrease with an increase of easy axis alignment, i.e. texturing, if there is a defect reducing the anisotropy near the grain boundaries [26,27]. We here consider a defect-free model and thus can expect results in agreement with Suss et al. and the Stoner–Wolfarth model, i.e. an increase in the coercivity with an increased easy axis alignment.

#### 4.3. Grain boundary width

To explore the influence of the grain boundary layer further, we next vary the thickness of this layer and study its influence on the coercivity and maximum energy product. We consider 9 different grain boundary layer widths, ranging from  $\delta_{\text{GB}} = 0$  nm to  $\delta_{\text{GB}} = 31.5$  nm. The base case with 25 grains but with increasing grain boundary widths are shown in Fig. 7.

The coercivity and the maximum energy product were determined from the computed hysteresis curves and are shown in Fig. 8. Besides the previous base model discussed above, we also consider a model with an easy axis alignment cone angle of  $\theta_{\text{cone}} = 1^\circ$ . As can be seen from the figure, the energy product is much more strongly affected by the increase in grain boundary width than the coercivity is. An explanation for this observation is that the magnetic field produced by the soft ferromagnetic grain boundary phase is not significantly

contributing to the external field, which is thus the primary factor in reaching the coercive field of the grains. It is thus not a surprise that the properties of the magnet worsen when the volume fraction of NdFeB material decreases. However, shown in Fig. 8 is the coercivity and the maximum energy product values for the case of  $\delta_{\text{GB}} = 0$  nm scaled by the volume fraction of the grain boundary phase for the given grain boundary width. As can be seen both the coercivity and the maximum energy product do not scale as the volume fraction of the grain boundary phase, although the maximum energy product do show a similar behavior as the simple volume fraction scaling.

#### 4.4. Grain boundary properties

In order to further investigate the properties of the grain boundary layer on the overall properties of the system, we systematically varied the exchange constant and the saturation magnetization of the grain boundary layer for the base case model. The values of  $A_0$  and  $M_s$  for the intergrain layer were varied independently and systematically from  $10^{-3}$  to  $10^1$  of the values for the base case, except combinations of high  $A_0$  and low  $M_s$  which were considered to be unrealistic material properties. Similarly as was done in the study of the influence of the exchange parameter,  $A_0$ , described in Section 4.1, the field steps size was decreased from 0.1 T to 0.01 T for the set of outermost data points in the high  $A_0$ , low  $M_s$  part of the data set shown in Fig. 9 to ensure that convergence was reached in all cases.

The determined coercivity and maximum energy product are shown in Fig. 9 as a color map, with the circles indicating the data points used for interpolation of the map. The material parameters corresponding to the white regions were not modeled, as stated above. As can be seen from the figure, the coercivity increases with lower  $A_0$  and  $M_s$  of the intergrain layer. This is expected as the less magnetic the intergrain



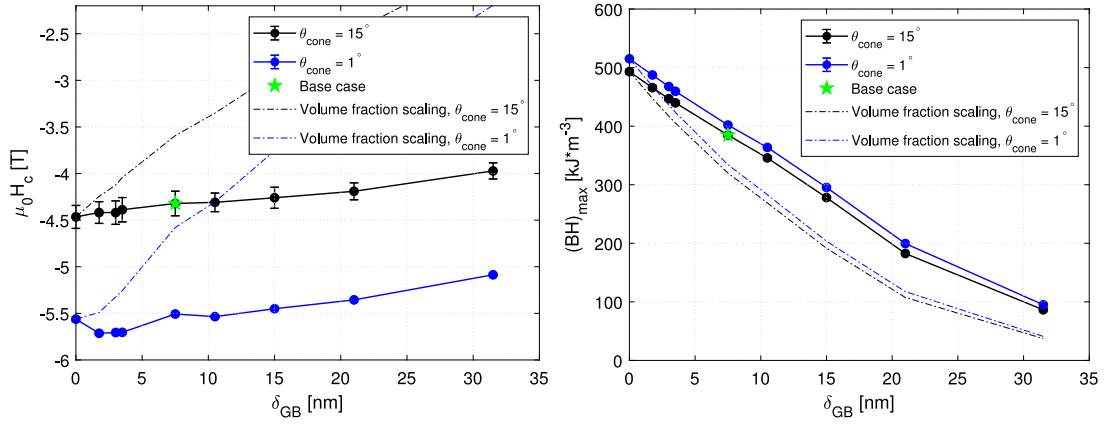


**Fig. 8.** The coercivity as function of the grain boundary width for two different cone opening angles for the easy axis direction of the grains. The volume fraction curves are the values for  $\delta_{GB} = 0$  nm scaled by the volume fraction of grain boundary material at the given value of  $\delta_{GB}$ .

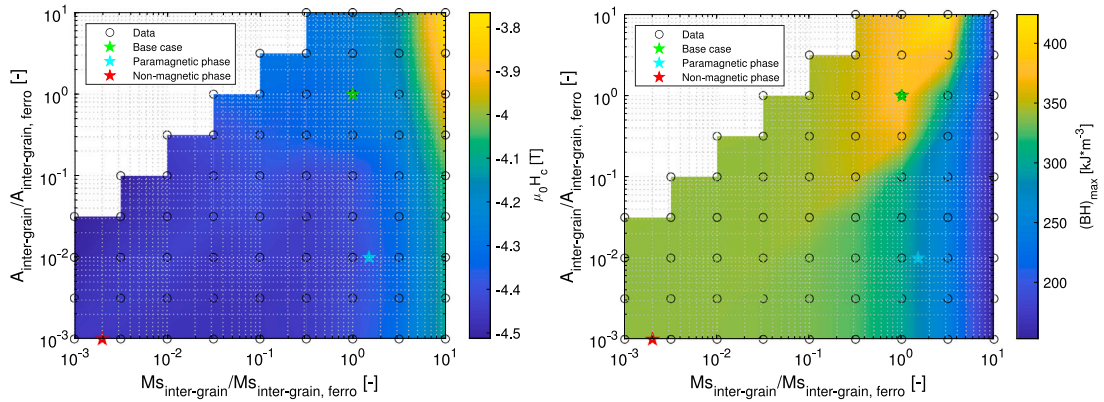


**Fig. 9.** (a) The coercivity and (b) the maximum energy product as function of the grain boundary  $M_s$  and the grain boundary  $A_0$  values normalized to their base line ferromagnetic values. The circles show the actual data points used to construct the interpolated surface.

layer is, the less the different magnetic grains couple across the grain boundary. In fact, being isotropic, the intergrain phase would demagnetize earlier and thus trigger demagnetization of the NdFeB grains due to the exchange coupling. However, it is of interest that the energy product apparently benefits from a strongly ferromagnetic material at the grain boundary. This can be interpreted as the grain boundary material generating a magnetic field that, if the external field is not strong enough to turn the grain boundary layer, positively contributes to the energy product of the system as a whole.

In the study of Toson et al. [6] three different sets of material parameters for the inter-grain phase are modeled. Besides the soft ferromagnetic phase listed previously, a paramagnetic phase with material properties  $\mu_0 M_s = 0.75$  T and  $A_0 = 0.077 \times 10^{-12}$  J/m<sup>1</sup>, as well as a non-magnetic phase with properties  $\mu_0 M_s = 0.001$  T and  $A_0 = 0.0077 \times 10^{-12}$  J/m are modeled. These material properties are also shown in Fig. 9. In that study there is a misorientation angle between the hard magnetic grains and the external field of 7–10 degrees. The study finds that modeling a paramagnetic phase for systems with 8 grains or more increases the coercivity by a factor of 1.4 on average, while if a non-magnetic phase is used the coercivity increases by a factor of 2.5. Estimating the coercivity for these material properties from Fig. 9 we here find a much smaller change in coercivity of only 1.02 and 1.06 respectively. However, it should be kept in mind that the simulations performed here have grains that can be internally misaligned, whereas this is not the case for Toson et al.

## 5. Discussion

Based on the above variation of the exchange constant, easy axis orientation, grain boundary width and grain boundary material properties, the results indicate that, while all of these can contribute to a reduction of coercivity of the system, the easy axis orientation has the largest influence. For this, a cone opening angle of  $\theta_{cone} = 15^\circ$  is enough to reduce the coercivity by 1 T. Regarding the maximum energy product, the width of the grain boundary layer, as well as the easy axis orientation were seen to have the largest influence, with the exchange constant only very weakly influencing the maximum energy product. Browns paradox is caused by combination of the previously mentioned factors, but the easy axis orientation seems to play the largest role among these.

Fig. 10 summarizes the impact of the various factors on the resulting coercivity and on the maximum energy product. The horizontal green line corresponds to the base case, whereas the bars indicate the change that occur when one of the properties is decreased or increased. As mentioned above, and as indicated in the graphs, the randomness of the easy axis orientation is the largest contribution affecting the coercivity. On the other hand, the thickness of the grain boundary region and the corresponding physical properties, i.e.  $A_0$  and  $M_s$ , are the factors that cause the largest change in the energy product.

Our study continues and expands several other investigations on micromagnetic simulations of hysteresis curves corresponding to NdFeB polycrystalline materials. In some cases the geometry is highly idealized, as in the work by Li et al. [28] investigating the effect of the grain boundary diffusion on an idealized structure composed of cubic grains arranged in a grid.

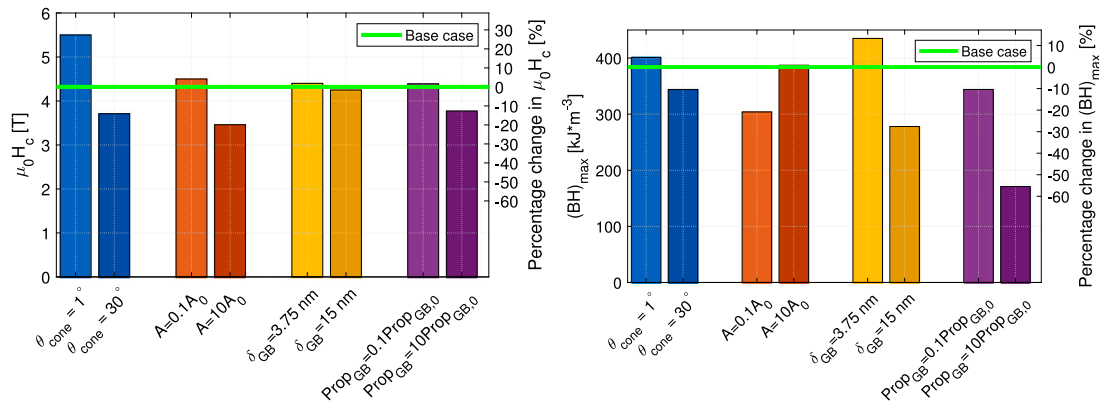


Fig. 10. A comparison of the influence of the different effects on the coercivity and the maximum energy product. The x-axis label indicate the parameter changed compared to the base model. The last x-axis label indicate a change in  $A_0$  and  $M_s$  of the grain boundary.

Other studies consider more realistic microstructure generation approaches based on Voronoi tessellations, similarly to the present work. For example, Liu et al. [29] investigate poly-crystalline magnets where some of the  $Nd_2Fe_{14}B$  crystal grains are replaced by  $Ce_2Fe_{14}B$ . They consider different proportions between the two materials. Moreover, they study the effect of the thickness of the grain boundary amorphous soft magnetic phase. In their work, this phase is modeled by assuming zero anisotropy and 10% of the saturation magnetization. Their calculations predict a reduction of the coercivity by  $\approx 0.1$  T as the thickness goes from 0 nm to 6 nm, which is of the same order of magnitude as the reduction shown in Fig. 8.

The work by Hong, et al. [30] analyzes a similar system, i.e. with secondary phase substitution of some of the  $Nd_2Fe_{14}B$  grains, while also considering the dependence of the coercivity on the saturation magnetization of the grain boundary phase and its thickness. Concerning the thickness, they found that for a non-magnetic grain boundary phase, i.e. with  $\mu_0 M_s = 0$  T, the coercivity is fairly independent of the thickness, while the remanent magnetization decreases by  $\approx 0.25$  T as the thickness increases from 4 nm to 14 nm. Conversely, when the grain boundary phase is magnetic, i.e. having almost the same value of  $M_s$  as the  $Nd_2Fe_{14}B$  grains, the coercivity decreases by  $\approx 1.2$  T as the thickness increases from 4 nm to 14 nm, while the remanent magnetization remains almost constant. Again, these results are in the same range as the reduction in  $H_c$  and  $(BH)_{max}$  predicted by our simulations as shown in Figs. 8 and 9.

Kim, et al. [31] focus on the effect of misalignment of the easy axis between different grains, finding that the coercivity decreases by  $\approx 34\%$  when the easy axes go from being perfectly aligned to each other to completely randomized, which is consistent with the  $\approx 45\%$  reduction predicted by our model and shown in Fig. 6.

Fischbacher et al. [32] analyzed the impact of the aspect ratio of the grains, the misorientation of the easy axes, thermal fluctuations and Dysprosium content in the grain boundary phase and its diffusion within the grains. Consistently with our results, they found that the misorientation of the easy axes and the magnetic properties of the grain boundary phase are then factors that affect the coercivity more significantly.

Our results are qualitatively in agreement with the aforementioned publications. However, a direct quantitative comparison between our investigations and previous works is not feasible, since there are too many independent input parameters affecting the results, e.g. aspect ratio of the grains, number of grains per unit volume, etc. Regarding the quantitative comparison of the coercivity computed by our model with the previously published results, the predictions of our study are in the same range as other studies, i.e.  $\approx 3$ – $5.5$  T.

## 6. Conclusions

The theoretical limit to the coercive force of magnets is known as the nucleation field and can be obtained from simple analytical arguments for single crystal magnets. However, the values of coercivity actually observed in NdFeB magnets are much lower than this theoretical limit. This inconsistency is referred to as Brown's paradox.

In reality, permanent magnets are not composed of a single crystal: on the contrary, the microstructure is composed of several crystal grains separated by a thin region occupied by soft-magnetic material. The crystallographic orientation does not have a perfect match between the different grains. Finally, the assumption of uniform magnetization does not remain valid when considering all but extremely small particles.

For all these reasons, it is not to be expected that the value of coercivity is aligned with the theoretical limit given by the nucleation field. In this work we performed a methodical analysis of the influence of all these different factors on the value coercivity and maximum energy product. Our investigation, based on variations of the exchange constant, easy axis orientation, grain boundary width and intergrain material properties, revealed that, while all of these can contribute to a reduction of coercivity, the easy axis orientation has the largest influence. Regarding the maximum energy product, the width of the grain boundary layer, as well as the easy axis orientation were seen to have the largest influence, with the exchange constant only very weakly influencing the maximum energy product. Our analysis thus methodically clarifies Brown's paradox.

## CRedit authorship contribution statement

**Rasmus Björk:** Conceptualization, Methodology, Investigation, Writing – original draft, Writing – review & editing, Visualization, Funding acquisition. **Andrea Roberto Insinga:** Conceptualization, Methodology, Writing – original draft, Writing – review & editing, Visualization.

## Declaration of competing interest

The authors declare that they have no known competing financial interests or personal relationships that could have appeared to influence the work reported in this paper.

## Data availability

All data shown in the work are directly available from Ref. [33]. This data repository contain all hysteresis curves for all simulations described in this work. The magnetization states, i.e. the magnetization of the individual tiles in each simulation for each field step in the hysteresis curve fills more than 500 Gb and therefore Ref. [33] only

contains the hysteresis curves at present. The magnetization states are available by request. Included in the data repository are also simulation scripts that can directly be used to recalculate the simulations described in this work using the open source MagTense framework [11].

## Acknowledgment

This work was supported by the Poul Due Jensen Foundation project on Browns paradox in permanent magnets, project nr. 2018-016.

## References

- [1] J.M.D. Coey, Permanent magnet applications, *J. Magn. Magn. Mater.* 248 (3) (2002) 441–456.
- [2] Hossein Sepehri-Amin, Satoshi Hirose, Kazuhiro Hono, Advances in Nd-Fe-B based permanent magnets, in: *Handbook of Magnetic Materials*, vol. 27, 2018, pp. 269–372.
- [3] Carlos J. Garcia-Cervera, Alexandre M. Roma, Adaptive mesh refinement for micromagnetics simulations, *IEEE Trans. Magn.* 42 (6) (2006) 1648–1654.
- [4] Johann Fischbacher, Alexander Kovacs, Markus Gusenbauer, Harald Oezelt, Lukas Exl, Simon Bance, Thomas Schrefl, Micromagnetics of rare-earth efficient permanent magnets, *J. Phys. D: Appl. Phys.* 51 (19) (2018) 193002.
- [5] H. Sepehri-Amin, T. Ohkubo, M. Gruber, T. Schrefl, K. Hono, Micromagnetic simulations on the grain size dependence of coercivity in anisotropic Nd-Fe-B sintered magnets, *Scr. Mater.* 89 (2014) 29–32.
- [6] P. Toson, G.A. Zickler, J. Fidler, Do micromagnetic simulations correctly predict hard magnetic hysteresis properties? *Phys. B: Condens. Matter* 486 (2016) 142–150.
- [7] H. Sepehri-Amin, T. Ohkubo, K. Hono, Micromagnetic simulations of magnetization reversals in Nd-Fe-B based permanent magnets, *Mater. Trans.* 57 (8) (2016) 1221–1229.
- [8] Alexander Kovacs, Johann Fischbacher, Harald Oezelt, Thomas Schrefl, Andreas Kaidatzis, Ruslan Salikhov, Michael Farle, George Giannopoulos, Dimitris Niarchos, Micromagnetic simulations for coercivity improvement through nanostructuring of rare-earth-free L10-FeNi magnets, *Ieee Trans. Magn.* 53 (11) (2017) 7920292.
- [9] Jae Hyeok Lee, Jinhyeok Choe, Shinwon Hwang, Sang Koog Kim, Magnetization reversal mechanism and coercivity enhancement in three-dimensional granular Nd-Fe-B magnets studied by micromagnetic simulations, *J. Appl. Phys.* 122 (7) (2017) 073901.
- [10] Hoyun Won, Yang Ki Hong, Minyeong Choi, Feng Yan, Gary J. Mankey, Xiao Han, Woncheol Lee, Chang Dong Yeo, Jongkook Lee, Taegyu Lee, Micromagnetic simulation of coercivity of alnico magnets, *Ieee Magn. Lett.* 12 (99) (2021) 9444156.
- [11] R. Bjørk, K.K. Nielsen, Magtense - A micromagnetism and magnetostatic framework, 2019, <http://dx.doi.org/10.11581/DTU:00000071>, <https://www.magtense.org>.
- [12] Rasmus Bjørk, Emil Blaabjerg Poulsen, Kaspar Kirstein Nielsen, Andrea Roberto Insinga, Magtense: A micromagnetic framework using the analytical demagnetization tensor, *J. Magn. Magn. Mater.* 535 (2021) 168057.
- [13]  $\mu$ mag standard problems, 2022, <https://www.ctcms.nist.gov/rdm/toc.html>. (Accessed 15 July 2022).
- [14] D. Givord, P. Tenaud, T. Viadieu, Coercivity mechanisms in ferrites and rare earth transition metal sintered magnets (smco5, Nd-Fe-B), *Ieee Trans. Magn.* 24 (2) (1988) 1921–1923.
- [15] Andrea Roberto Insinga, Emil Blaabjerg Poulsen, Kaspar Kirstein Nielsen, Rasmus Bjørk, A direct method to solve quasistatic micromagnetic problems, *J. Magn. Magn. Mater.* 510 (2020) 166900.
- [16] M. Maicas, E. López, M.C. Sánchez, C. Aroca, P. Sánchez, Magnetostatic energy calculations in two- and three-dimensional arrays of ferromagnetic prisms, *Ieee Trans. Magn.* 34 (3) (1998) 601–607.
- [17] Emil Blaabjerg Poulsen, Andrea Roberto Insinga, Rasmus Bjørk, Direct exchange calculation for unstructured micromagnetic meshes, *J. Magn. Magn. Mater.* 551 (2022) 169093.
- [18] H. Sepehri-Amin, T. Ohkubo, T. Shima, K. Hono, Grain boundary and interface chemistry of an Nd-Fe-B-based sintered magnet, *Acta Mater.* 60 (3) (2012) 819–830.
- [19] Yasukazu Murakami, T. Tanigaki, T.T. Sasaki, Y. Takeno, H.S. Park, T. Matsuda, T. Ohkubo, K. Hono, D. Shindo, Magnetism of ultrathin intergranular boundary regions in Nd-Fe-B permanent magnets, *Acta Mater.* 71 (2014) 370–379.
- [20] Teruo Kohashi, Kumi Motai, Takeshi Nishiuchi, Satoshi Hirose, Magnetism in grain-boundary phase of a NdFeB sintered magnet studied by spin-polarized scanning electron microscopy, *Appl. Phys. Lett.* 104 (23) (2014) 232408.
- [21] W.F. Brown, Criterion for uniform micromagnetization, *Phys. Rev.* 105 (5) (1957) 1479–1482.
- [22] H. Kronmüller, K.-D. Durst, M. Sagawa, Analysis of the magnetic hardening mechanism in RE-FeB permanent magnets, *J. Magn. Magn. Mater.* 74 (3) (1988) 291–302.
- [23] Yutaka Matsuura, Jun Hoshijima, Rintaro Ishii, Relation between Nd<sub>2</sub>Fe<sub>14</sub>B grain alignment and coercive force decrease ratio in NdFeB sintered magnets, *J. Magn. Magn. Mater.* 336 (2013) 88–92.
- [24] T.T. Sasaki, T. Ohkubo, Y. Takada, T. Sato, A. Kato, Y. Kaneko, K. Hono, Formation of non-ferromagnetic grain boundary phase in a Ga-doped Nd-rich Nd-Fe-B sintered magnet, *Scr. Mater.* 113 (2016) 218–221.
- [25] Jiangnan Li, Hossein Sepehri-Amin, Taisuke Sasaki, Tadakatsu Ohkubo, Kazuhiro Hono, Most frequently asked questions about the coercivity of Nd-Fe-B permanent magnets, *Sci. Technol. Adv. Mater.* 22 (1) (2021) 386–403.
- [26] Dieter Suss, Thomas Schrefl, Josef Fidler, Micromagnetics simulation of high energy density permanent magnets, *IEEE Trans. Magn.* 36 (5) (2000) 3282–3284.
- [27] Hossein Sepehri-Amin, Satoshi Hirose, Kazuhiro Hono, Advances in Nd-Fe-B based permanent magnets, in: *Handbook of Magnetic Materials*, vol. 27, Elsevier, 2018, pp. 269–372.
- [28] W. Li, Q. Zhou, L.Z. Zhao, Q.X. Wang, X.C. Zhong, Z.W. Liu, Micromagnetic simulation of anisotropic grain boundary diffusion for sintered Nd-Fe-B magnets, *J. Magn. Magn. Mater.* 451 (2018) 704–709.
- [29] D. Liu, T.Y. Zhao, R. Li, M. Zhang, R.X. Shang, J.F. Xiong, J. Zhang, J.R. Sun, B.G. Shen, Micromagnetic simulation of the influence of grain boundary on cerium substituted Nd-Fe-B magnets, *Aip Adv.* 7 (5) (2017) 056201.
- [30] Yuan Hong, Gang Wang, Nora M. Dempsey, Dominique Givord, Dechang Zeng, Micromagnetic simulation of the effect of grain boundaries and secondary phases on the magnetic properties and recoil loops of hot-deformed NdFeB magnets, *J. Magn. Magn. Mater.* 491 (2019) 165328.
- [31] Sang Koog Kim, Shinwon Hwang, Jae Hyeok Lee, Effect of misalignments of individual grains' easy axis on magnetization-reversal process in granular NdFeB magnets: A finite-element micromagnetic simulation study, *J. Magn. Magn. Mater.* 486 (2019) 165257.
- [32] J. Fischbacher, A. Kovacs, Lukas Exl, Julian Kühnel, Eduard Mehofer, H. Sepehri-Amin, T. Ohkubo, K. Hono, T. Schrefl, Searching the weakest link: Demagnetizing fields and magnetization reversal in permanent magnets, *Scr. Mater.* 154 (2018) 253–258.
- [33] R. Bjørk, A.R. Insinga, Data for article explaining browns paradox in NdFeB magnets from micromagnetic simulations, 2023, <http://dx.doi.org/10.11583/DTU.21558276>, data.dtu.dk.